

Supporting Information:

Macroscopic Salt Rejection through Electrostatically Gated Porous Graphene

Roman M. Wyss,^{†,||} Tian Tian,^{‡,||} Khadija Yazda,[¶] Hyung Gyu Park,^{*,¶,§} and
Chih-Jen Shih^{*,‡}

[†]*Institute of Soft Materials Department of Material Sciences, Eidgenössische Technische Hochschule (ETH) Zürich, Vladimir-Prelog-Weg 1-5, Zürich CH-8093, Switzerland.*

[‡]*Institute for Chemical and Bioengineering Department of Chemistry and Applied Biosciences, Eidgenössische Technische Hochschule (ETH) Zürich, Vladimir-Prelog-Weg 1-5, Zürich CH-8093, Switzerland.*

[¶]*Nanoscience for Energy Technology and Sustainability, Department of Mechanical and Process Engineering, Eidgenössische Technische Hochschule (ETH) Zürich, Tannenstrasse 3, Zürich CH-8092, Switzerland.*

[§]*Mechanical Engineering, Pohang University of Science and Technology (POSTECH), 77 Cheongam-ro, Nam-gu, Pohang, Gyeongbuk, Republic of Korea.*

^{||}*R. M. S. and T. T. contributed equally to this work*

E-mail: iduserpark@gmail.com; chih-jen.shih@chem.ethz.ch

S1 Graphene membrane manufacturing and results.

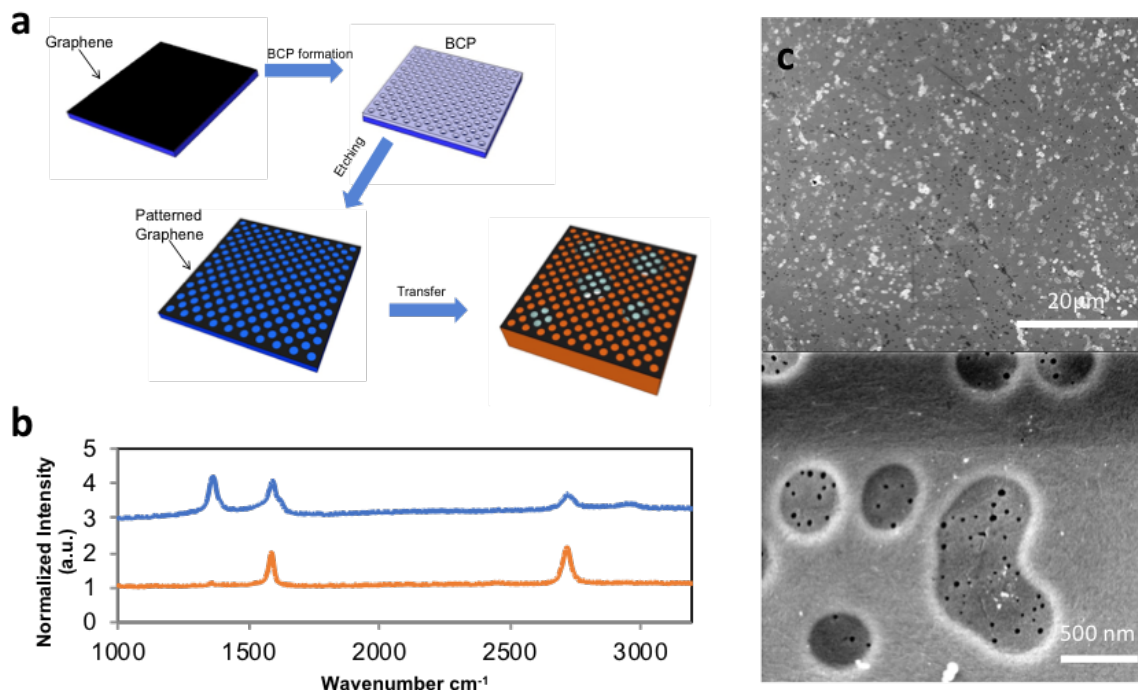


Figure S1: **a.** Schematic of manufacturing process for patterning of double layer graphene. Graphene is synthesized and transferred to a substrate (glass slide) to yield a double layer. s-BCP is spin-coated and annealed in vacuum to undergo microphase separation, followed by plasma etch and wet etching yielding a porous polystyrene (PS) mask. Anisotropic etching of the mask leads to patterning the underlying graphene, PS is removed by thermal annealing. The porous graphene is then transferred to a substrate (e.g. PCTE). **b.** Raman spectra of graphene before (orange curve) and after (blue curve) patterning. An increase of the D-peak at 1350 cm^{-1} indicates the formation of defects and edges. The spectra have been normalized to the G-peak intensity and offset for better comparison. **c.** SEM graph of patterned graphene on PCTE at lower (top) and higher (bottom) magnifications.

S2 Supplementary Section 2. Ion diffusion measurement and calculation

The ion diffusion through b-PCTE has been performed using a sample sandwiched between two layers of Aluminum tape where the edges have been sealed using water-resistant epoxy (ACS Marine Epoxy) to avoid interlayer leakage pathways.^{S2} The sample was inserted in the fixture

Table S1: Different diffusivities for the anions and cations of the salts used in this work.^{S1} The theoretical diffusion through PCTE can be calculated using Eq. 1 in the main text and the diffusivities of the respective anion and cation.

Salt	D ($10^9 \text{ m}^2 \cdot \text{s}^{-1}$)
K^+	1.95
Na^+	1.33
Li^+	1.03
SO_4^{2-}	1.06
Ca^{2+}	0.79
Mg^{2+}	0.7
$\text{Fe}[(\text{CN})_6]^{3-}$	0.90
Cl^-	2.03

following the same wetting procedure described in the main text Methods and was kept wet for the entire series of experiments.

The conductivity increases s ($\text{mS} \cdot \text{cm}^{-1} \cdot \text{d}^{-1}$) is converted into ion permeation rates J_{PCTE} ($\text{mol} \cdot \text{m}^{-2} \cdot \text{s}^{-1}$) by use of a calibration factor c_f , the volume of LCR (V_{LCR}), the area of the membrane A and the time t as:

$$J_{\text{PCTE}} = \frac{sV_{\text{LCR}}}{c_f A t} \quad (1)$$

The calibration factors for all salts have been obtained by a linear fit of conductivity versus concentration for 4 solutions with concentrations from 10^{-4} M to 10^{-2} M and extracting the resulting slope. The rest of the factors are $V_{\text{LCR}} = 7.33 \text{ mL}$, $A = 9 \times 10^{-6} \text{ m}^2$. Table S2 shows the averaged conductivity increase s , the extracted calibration factors c_f and the resulting ion permeation rates using Eq. 1. The values from this table are shown in main text Fig.2b (blue bars).

Table S2: Extracted slope s as an averaged result from 3 consecutive measurements, the calibration factors c_f and the resulting ion permeation J_{PCTE} through b-PCTE membranes for all salts.

Salt	s ($\text{mS} \cdot \text{cm}^{-1} \cdot \text{d}^{-1}$)	c_f ($\text{mS} \cdot \text{cm}^{-1} \cdot \text{mol}^{-1} \cdot \text{ml}$)	J_{PCTE} ($10^6 \text{ mol} \cdot \text{m}^{-2} \cdot \text{s}^{-1}$)
KCl	$1.51 \pm 0.27 \times 10^{-2}$	106	1.34 ± 0.24
NaCl	$9.90 \pm 0.17 \times 10^{-3}$	91	1.02 ± 0.02
LiCl	$6.03 \pm 0.80 \times 10^{-3}$	83	0.682 ± 0.090
CaCl_2	$1.25 \pm 0.1 \times 10^{-2}$	149	0.789 ± 0.063
MgSO_4	$8.80 \pm 1.2 \times 10^{-3}$	130	0.633 ± 0.084
$\text{K}_3[\text{Fe}(\text{CN})_6]$	$2.40 \pm 0.28 \times 10^{-2}$	395	0.575 ± 0.063
K_2SO_4	$1.98 \pm 0.20 \times 10^{-2}$	258	0.722 ± 0.073

S3 Control experiment with copper tape

We make sure that the applied voltage is effectively applied via the graphene membrane and not through leakage directly coupling the coppertape to the ionic solution. For this, we use a device as in Fig.1a, omitting the graphene and measuring the current through the membrane with the Autolab electrochemical workstation using the membrane as working electrode and a platinum wire as counter/reference electrode 3.5 cm apart in 0.1 mM KCl. When no graphene is inserted in the device, a current in the baseline range (~ 0.1 nA) is observed, indicating no current passing from the membrane. However, if graphene is inserted, a current in the range of $\sim 10 - 100$ nA is measured. If the copper tape is in contact with the solution when omitting the Kapton tape, the current increases to $\sim 1 - 10$ μ A, independent of the exposed area of the copper tape to the solution.

S4 KCl Debye length and conductivity

Table S3 gives an overview about the measured conductivities and their calculated Debye length values for KCl. The information is used to plot the ξ versus c_0 curve.

Table S3: Conductivity and calculated Debye lengths of various KCl concentrations in order to obtain rectification versus concentration curves.

c_0 (mM)	Conductivity ($\text{mS}\cdot\text{cm}^{-1}$)	λ_D (nm)
0.1	1.90×10^{-2}	30.4
0.33	5.41×10^{-2}	16.0
1	1.33×10^{-1}	10.0
3.3	5.13×10^{-1}	6.0
10	1.08	3.3

S5 Further details of the numerical simulation

The numerical simulations were carried out using COMSOL Multiphysics 5.3a. The simulation domain is shown in Fig.S2. To simplify the geometry, we use axial symmetric coordinate system. The radius L and height H of both HCR and LCR are set to $20 R_G$, the radius of the nanopore. The

potential at the bottom of the LCR and the center of the graphene domains are set to be 0 and ψ_G , respectively. The potential at the end of HCR is not set explicitly, but rather determined through the Poisson equation with no flux boundary condition $\mathbf{D}^{\text{norm}} = 0$. The relative permittivity in the HCR and LCR is set as $\varepsilon = 78$. The relative permittivity of the Stern layer is set to $\varepsilon_H = 20$ ^{S3} and for the graphene domain we set the relative permittivity as a large number (e.g. 10^5) for a better convergence of the solver. For the transport of diluted ionic species, we use the PNP equations to describe the diffusion and drift of the ions, which can be further unified by the gradient of electrochemical potential, as described in the main text. The initial values of the electrolyte is set to c_0 in HCR and $0.1 c_0$ in LCR. At the ends of the cells in the z-direction, we use the inlet boundaries conditions for the concentration of electrolytes, that the concentration on these boundaries remains the same with the initial value, due to the effective mixing in the experimental setup.

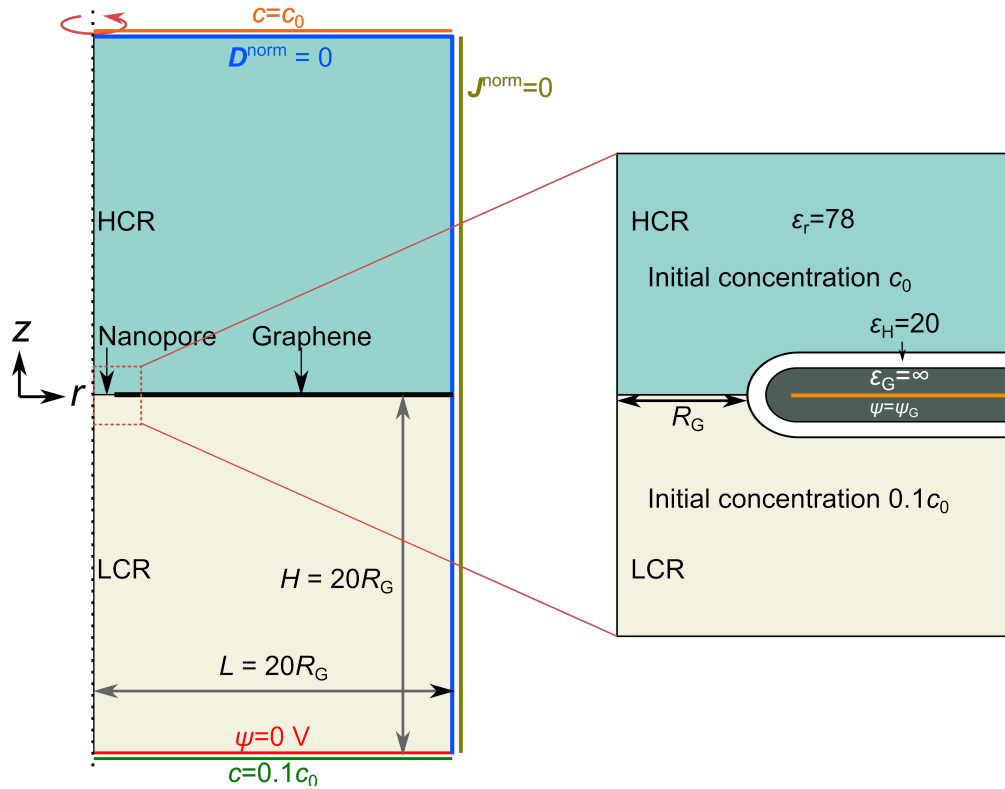


Figure S2: Scheme of the simulation domain used. Left: geometry of the whole simulation domain. Right: configuration near the graphene nanopore, corresponding to the red rectangle on the left side.

The transport of ionic species is described by the steady-state Nernst-Planck equation:

$$\nabla \cdot \mathbf{J}_i = -\nabla \cdot \left(\frac{D_i}{k_B T} c_i N_A \nabla \mu_i \right) = -\nabla \cdot \left(\frac{D_i}{k_B T} c_i N_A [k_B T \nabla \ln x_i + z_i e \nabla \psi] \right) = 0 \quad (2)$$

$$x_i = \frac{c_i}{\sum_i c_i + c_{\text{H}_2\text{O}}} \quad (3)$$

The potential distribution within the whole simulation domain is described by the Poisson equation:

$$\nabla \cdot (\varepsilon_m \varepsilon_0 \nabla \psi) = -N_A e \sum_i c_i z_i \quad (4)$$

Where ε_m is the relative permittivity of domain m. The contribution of mobile charges is only valid in the solution domain. The use of a large ε_G ensures that the potential in the whole simulation domain can be solved continuously.

To simulate the applied external bias V_G , we set the value of ψ_G explicitly and extract the charge σ_G by:

$$\sigma_G = -\frac{\int_{\Omega} z_i c_i N_A e d^3 \Omega}{S_G} \quad (5)$$

and V_G is then calculated by:

$$V_G = \Delta \phi_G + \psi_G \quad (6)$$

$$\sigma_G = \int_0^{\Delta \phi_G} \frac{1}{C_Q(\phi_G)} d\phi_G \quad (7)$$

where the quantum capacitance $C_Q = \partial \sigma_G / \partial \phi_G$ is calculated by Eq. 8 in main text.

Note that due to the existence of electron traps on graphene due to fabrication process, the induced charge traps on graphene effectively reduce the charge density on graphene and greatly attenuate the surface potential on graphene, as illustrated in Fig.S3. This effect is universally observed in CVD-graphene-based field effect transistors in air, while the mechanism is fully understood yet. In view of this, we only simulate the situation where $V_G > 0$ for the salt rejection mechanism. The trend that ξ is almost independent of V_G when $V_G < 0$ can be qualitatively explained by the existence of surface charge traps as stated above. We have also tested the mesh-

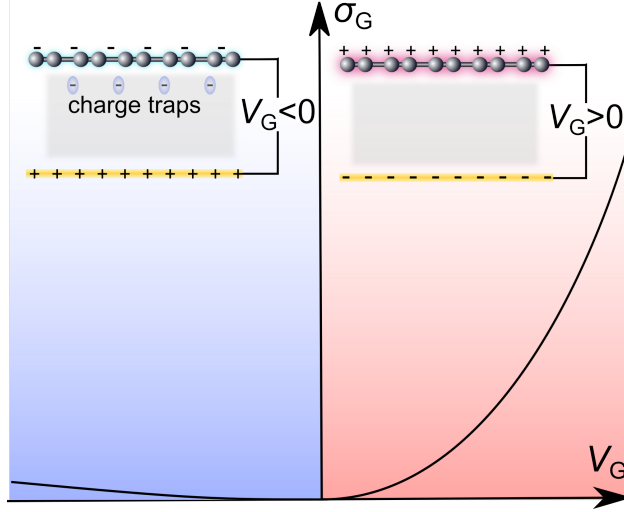


Figure S3: Schematic illustration of the origin of the asymmetric rectification with respect to V_G . Due to the existence of surface charge traps at negative V_G , the graphene is less charged compared to the positive V_G .

independency of our solutions. As show in in Fig. S4a, we use two parameters to control the refinement of the mesh entities: (i) triangle mesh division N_{div} , giving the smallest triangle mesh size δ_G/N_{div} , where δ_G is the thickness of graphene, and (ii) division of mesh N_b , on the boundary $0 < r < R_G; z = 0$. The solution convergence is evaluated by the mean absolute error (MAE) of anion flux \mathbf{J}_z on the boundary $0 < r < R_G; z = 0$, as shown in Fig. S4b. The solution of the PNP model is sensitive to the value N_b , and can be regarded numerically converged when $N_b > 100$. Combining the calculation effort and numerical precision, we adapt the value $N_{\text{div}} = 5$ and $N_b = 100$ in our simulations.

S6 Further numerical simulation results

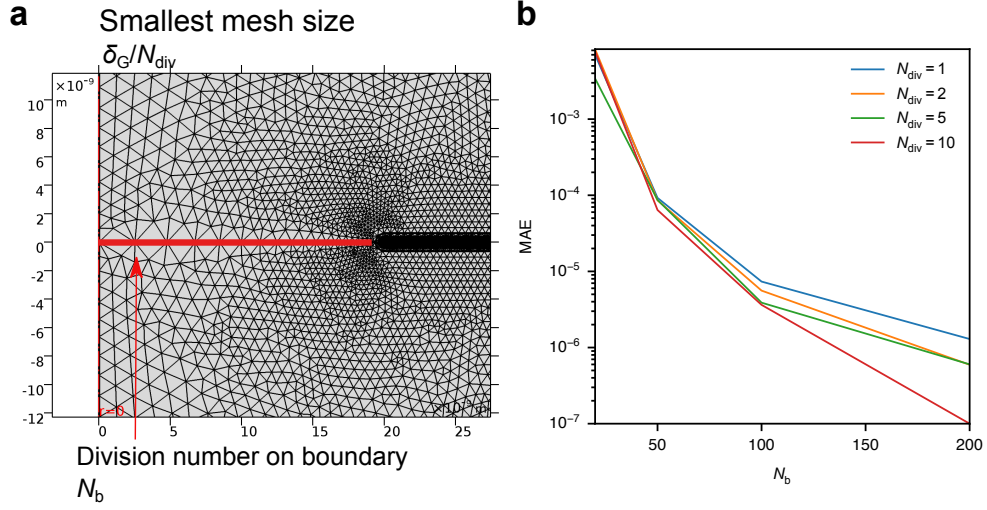


Figure S4: Mesh independence of the solution. **a.** Scheme of the mesh refinement near the graphene pore. The values N_{div} and N_b controls the size of mesh along the boundary $z = 0, 0 < r < R_G$ (shown in red). **b.** Mean absolute error (MAE) of the anion flux J_z along the boundary $z = 0, 0 < r < R_G$. The error is more sensitive to N_b than N_{div} .

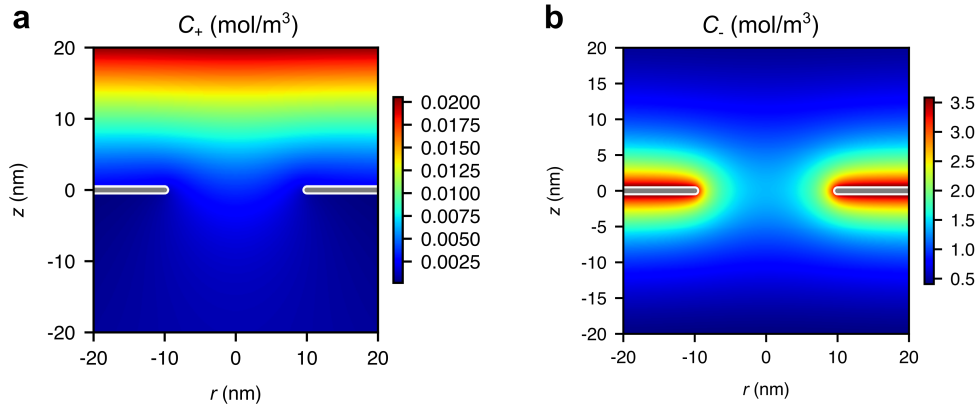


Figure S5: Cation concentration c_+ (**a.**) and anion concentration c_- (**b.**) near the graphene nanopore for KCl solution at 0.1 mM. Depletion of cation and accumulation of anion can be observed near the graphene surface.

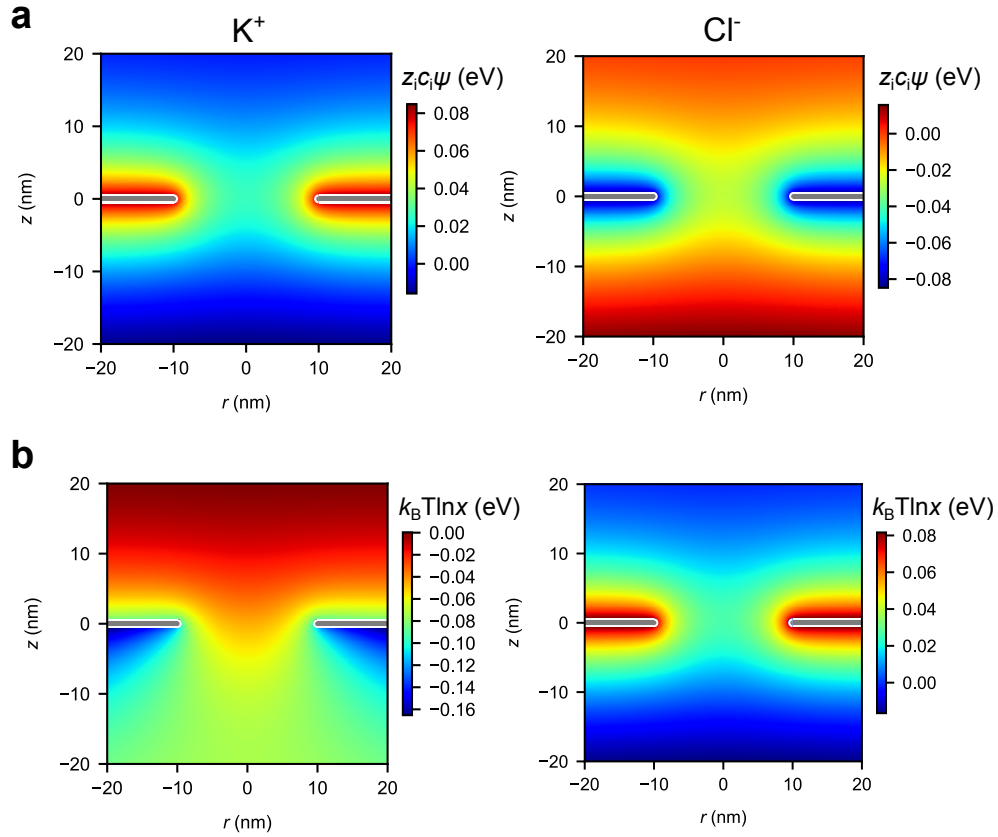


Figure S6: Decomposition of electrochemical potential near a nanopore corresponding to Fig.4 in main text. **a.** The electrostatic (drift) contribution to the electrochemical potential for cation (left) and anion (right) and **b.** The concentration (diffusion) contribution to the electrochemical potential for cation (left) and anion (right). The relative small order of magnitude for anion electrochemical potential is caused by the balance between the diffusion and drift for anion.

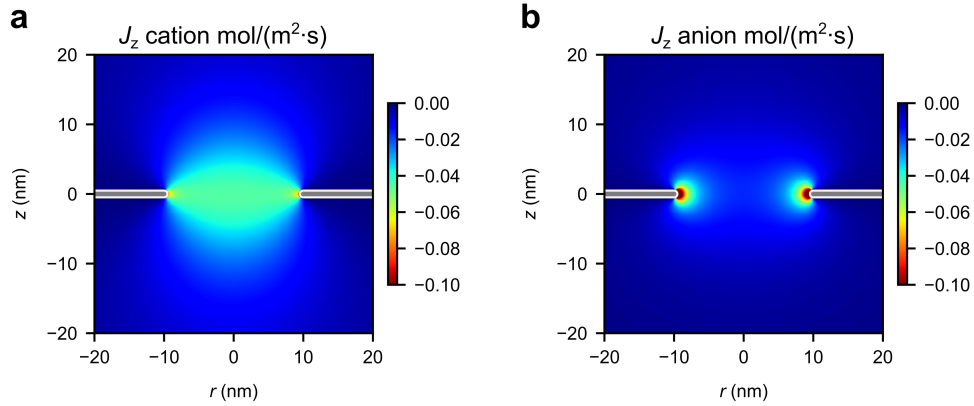


Figure S7: z-component flux J_z of cation (a.) and anion (b.) near the graphene nanopore corresponding to Figure 4b in main text. The pathways for the different ions can be spatially distinguished: the flux of cation passes mostly through the center of the graphene nanopore while the anion passes mainly through the edge. The analysis is in consistent with the gradient of chemical potential as shown in the main text Fig.4b.

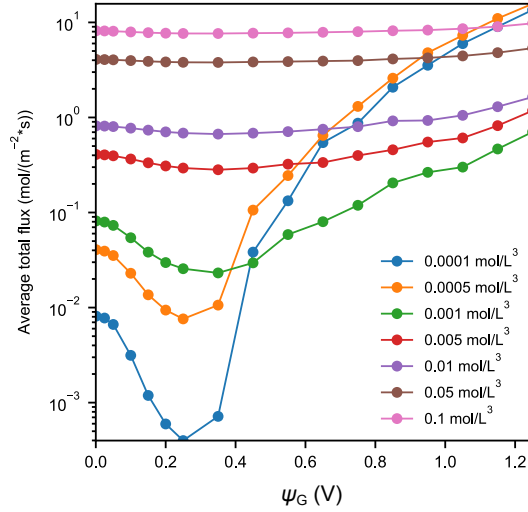


Figure S8: Average total flux J_z in the nanopore as a function of ψ_G at different concentrations. The range of ψ_G is larger than the experimentally achievable value. The rectification of flux becomes weaker after a certain level of ψ_G is reached. Further increasing the surface potential of graphene may even enhance the transportation of ions, which is similar to the cases of ionic transistors.

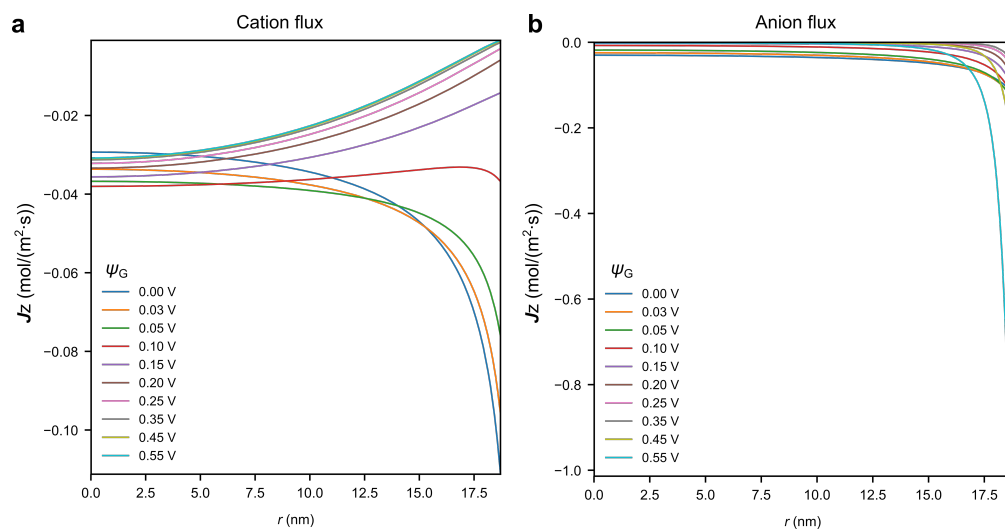


Figure S9: Spatial distribution of J_z as a function of r in a 20 nm nanopore at different levels of ψ_G (larger than experimentally achievable values) for cation (**a.**) and anion (**b.**). The cation flux becomes nearly saturated with increasing ψ_G , while the flow of anion near the pore edge becomes much larger. The drastic increase of pore-bounded anion flux is caused by the accumulation of anions near the graphene surface, and in turn causes the increasing of total flux as seen in Fig.S8.

S7 Conductivities and Debye length for all salts

In Table S3, the conductivities and calculated Debye lengths for 6 salts are shown. At the same concentration, the higher ionic strength of the multivalent salts leads to a reduction of the respective Debye lengths.

Table S4: Conductivity and λ_D of various salts.

Solution	Conductivity ($\text{mS}\cdot\text{cm}^{-1}$)	λ_D (nm)
0.1 mM NaCl	1.80×10^{-2}	30.4
0.1 mM LiCl	1.58×10^{-2}	30.4
0.1 mM CaCl_2	2.19×10^{-2}	17.2
0.1 mM MgSO_4	3.27×10^{-2}	15.2
0.1 mM K_2SO_4	4.16×10^{-2}	17.2
0.1 mM $\text{K}_3[\text{Fe}(\text{CN})_6]$	5.95×10^{-2}	12.4

References

- (S1) Vanysek, P. Ionic conductivity and diffusion at infinite dilution. *CRC handbook of chemistry and physics* **2000**, 83.
- (S2) Choi, K.; Droudian, A.; Wyss, R. M.; Karl-Philipp, S.; Park, H. G. Multifunctional Wafer-Scale Graphene Membranes for Fast Ultrafiltration and High Permeation Gas Separation. *Sci. Adv.* **2018**, *in press*.
- (S3) Conway, B. E.; Bockris, J. O.; Ammar, I. A. The dielectric constant of the solution in the diffuse and Helmholtz double layers at a charged interface in aqueous solution. *Trans. Faraday Soc.* **1951**, 47, 756–766.